Supplementary Materials

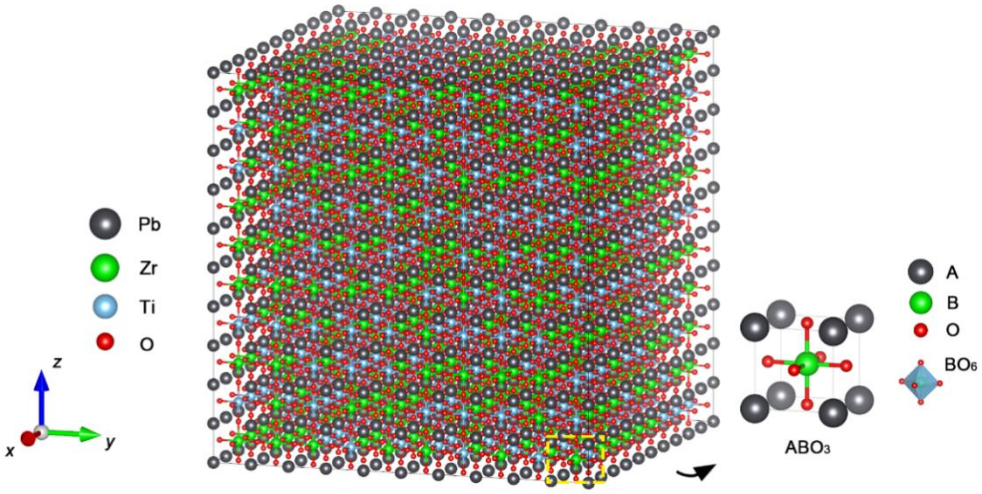
Dynamic octahedral freezing and polarization rotation in lead zirconate titanate

Xiaohan Huang[1], Yihan Nie[2], Haifei Zhan[1,3,*], Gang Zhang[4,5], Chaofeng Lü[1,6,*]

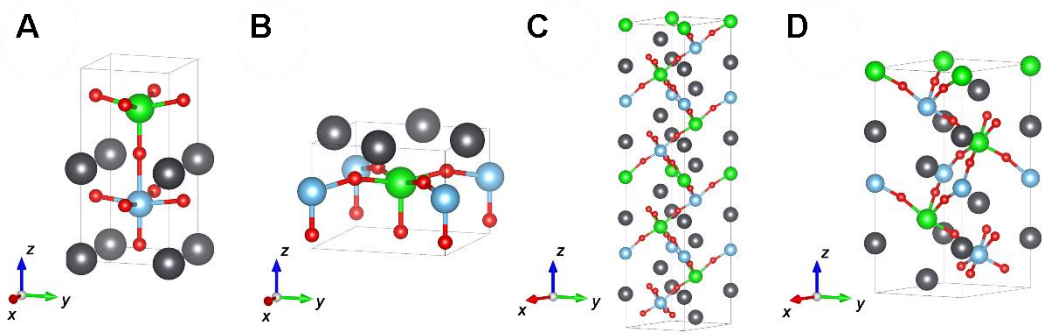
[1]College of Civil Engineering and Architecture, Zhejiang University, Hangzhou 310058, Zhejiang, China.
[2]School of Power and Energy, Northwestern Polytechnical University, Xi'an 710072, Shaanxi, China.
[3]School of Mechanical, Medical and Process Engineering, Queensland University of Technology (QUT), Brisbane QLD 4001, Australia.
[4]School of Materials Science and Engineering, Beijing Institute of Technology, Beijing 100081, China.
[5]School of Aeronautics and Astronautics, Zhejiang University, Hangzhou 310058, Zhejiang, China.
[6]Faculty of Mechanical Engineering & Mechanics, Ningbo University, Ningbo 315211, Zhejiang, China.

[*]**Correspondence to:** Prof. Haifei Zhan, College of Civil Engineering and Architecture, Zhejiang University, Hangzhou 310058, Zhejiang, China. E-mail: zhan_haifei@zju.edu.cn; Prof. Chaofeng Lü, Faculty of Mechanical Engineering & Mechanics, Ningbo University, Ningbo 315211, Zhejiang, China. E-mail: lucf@nbu.edu.cn

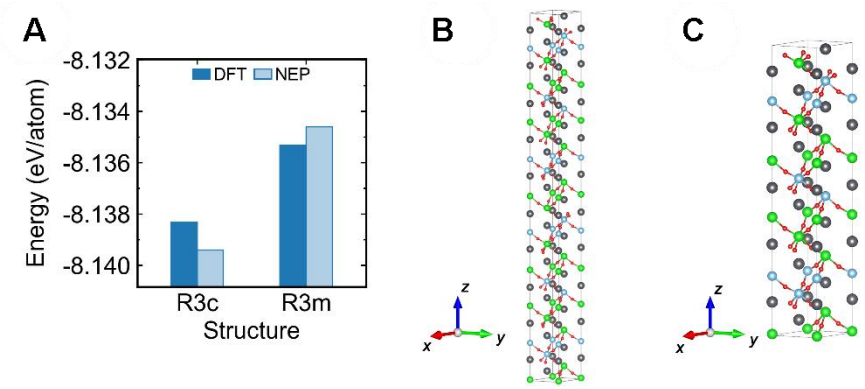
Supplementary Figures



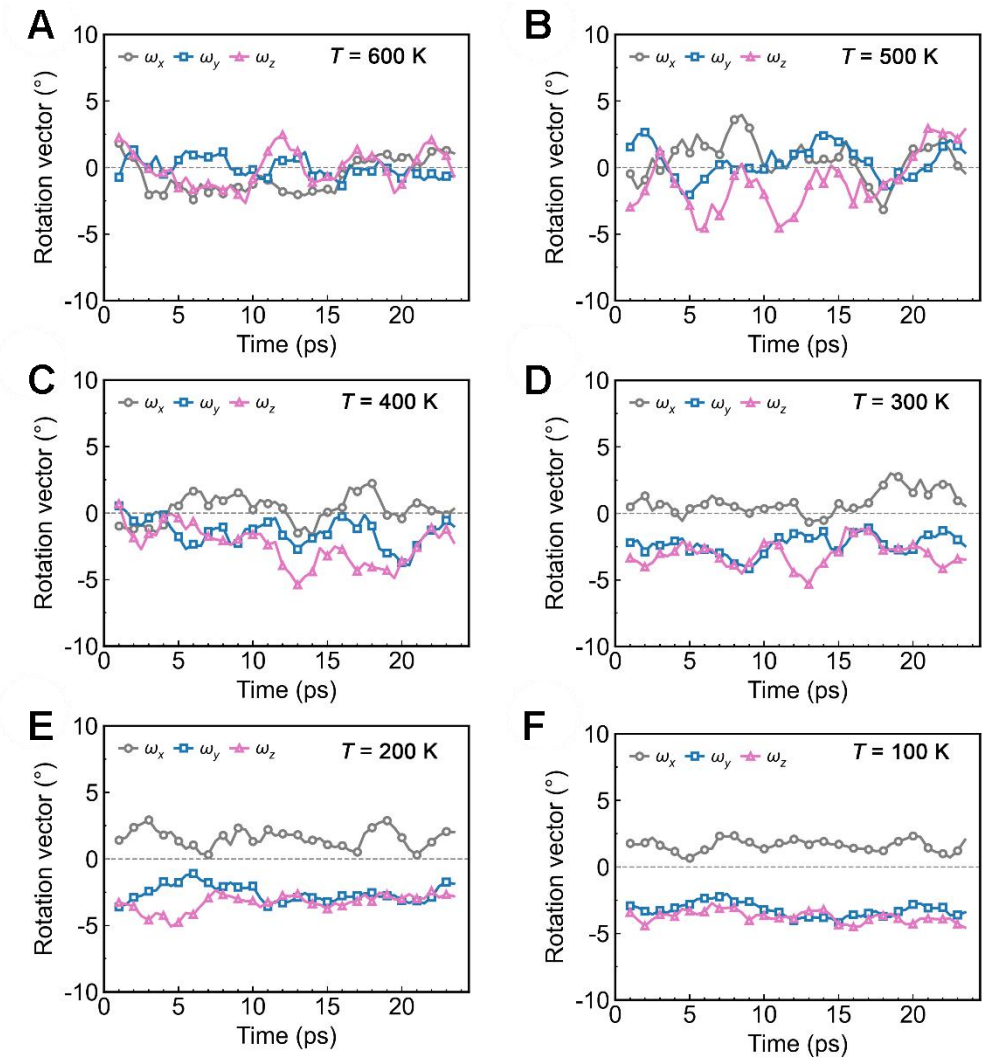
Supplementary Figure 1. Full atomic snapshot of the 10×10×10 $Pb(Zr_{0.5}Ti_{0.5})O_3$ supercell containing 5000 atoms (1000 Pb, 500 Ti, 500 Zr, 3000 O). Ti and Zr cations are randomly disordered over the B-site.



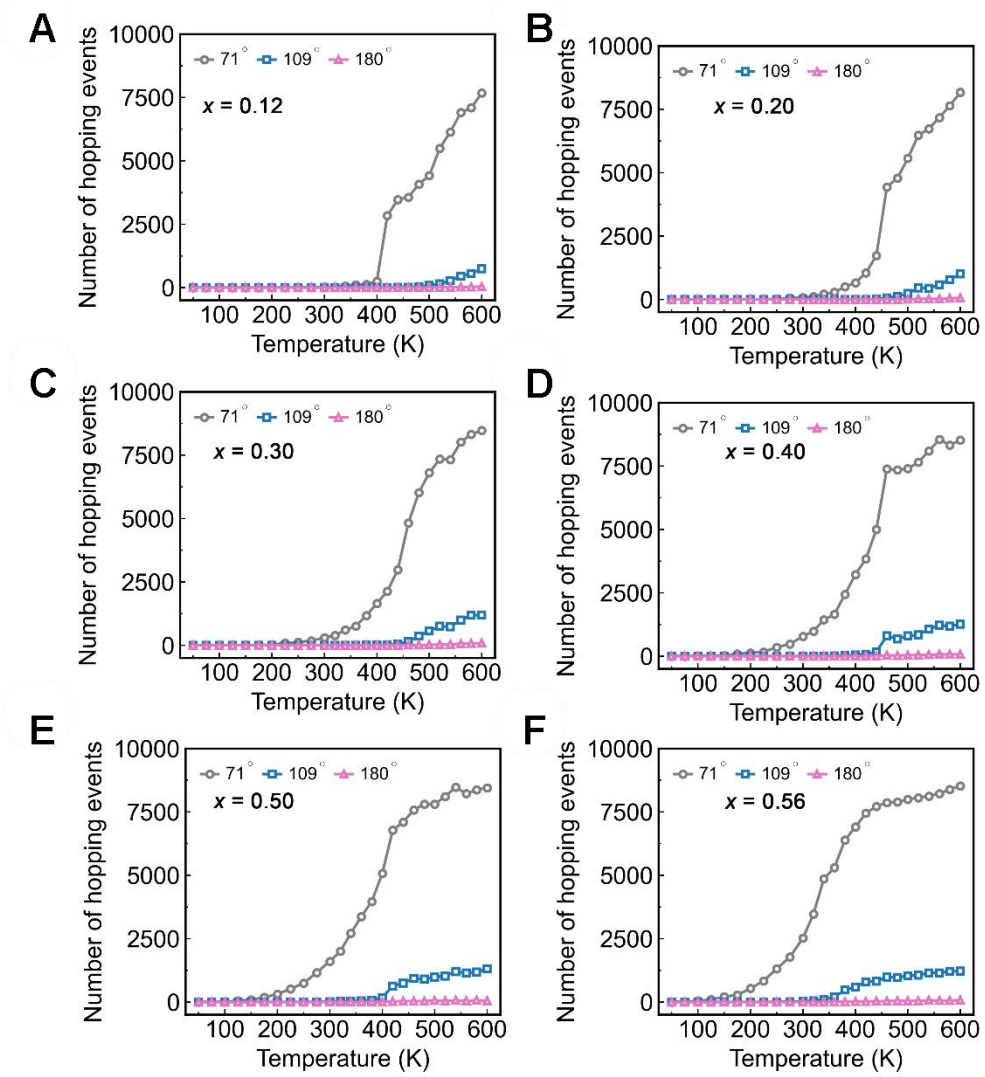
Supplementary Figure 2. Atomic structures used for the energy comparison at x = 0.50. (A-D) Structural models of $Pb(Zr_{0.5}Ti_{0.5})O_3$ corresponding to P4mm1, P4mm2, R3c and R3m, respectively, whose DFT and NEP energies are compared in Figure 1F. P4mm1 and P4mm2 denote tetragonal structures with different Zr/Ti arrangements.



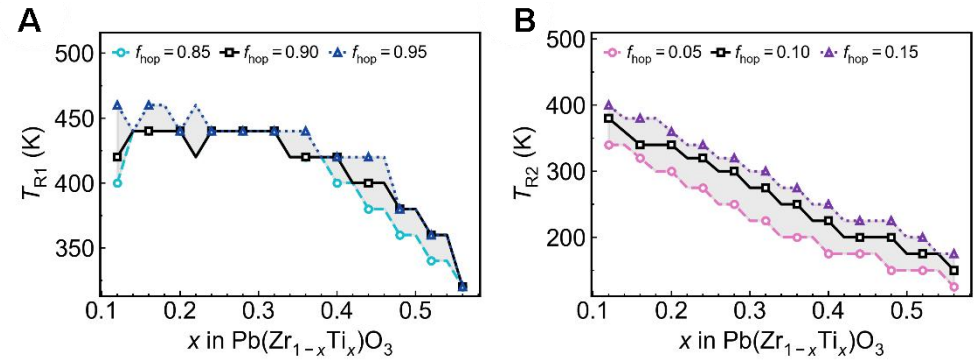
Supplementary Figure 3. DFT and NEP energies of competing rhombohedral structures at $x = 0.40$. (A) Energies per atom of the R3c and R3m structures calculated using DFT and NEP. Both methods predict a lower energy for R3c, with an energy separation ($\Delta E = E_{R3m} - E_{R3c}$) of 2.99 meV/atom for DFT and 4.80 meV/atom for NEP. (B and C) unit-cell structures used for the comparison: (B) R3c; (C) R3m.



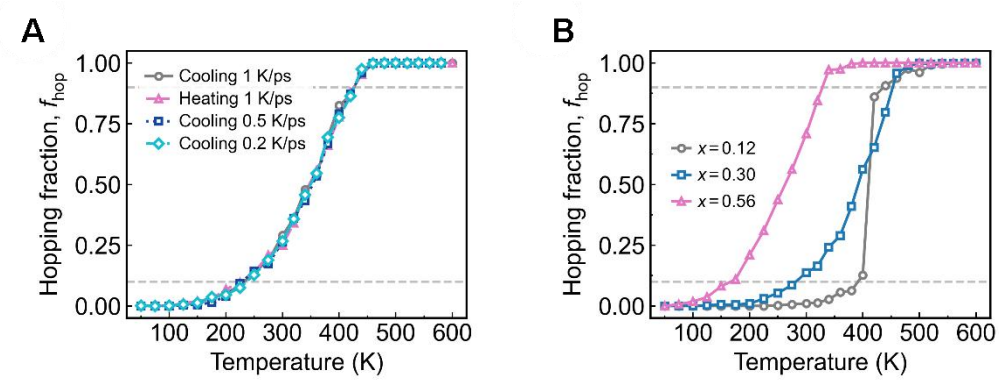
Supplementary Figure 4. Time evolution of a local oxygen-octahedral rotation vector in $Pb(Zr_{0.6}Ti_{0.4})O_3$. (A-F) Cartesian components of the rotation vector of a selected oxygen octahedron at 600, 500, 400, 300, 200 and 100 K, respectively, over the final 25 ps of the sampled trajectory. A 2-ps moving average is applied to each component. The vectors are shown without multiplication by the antiphase factors.



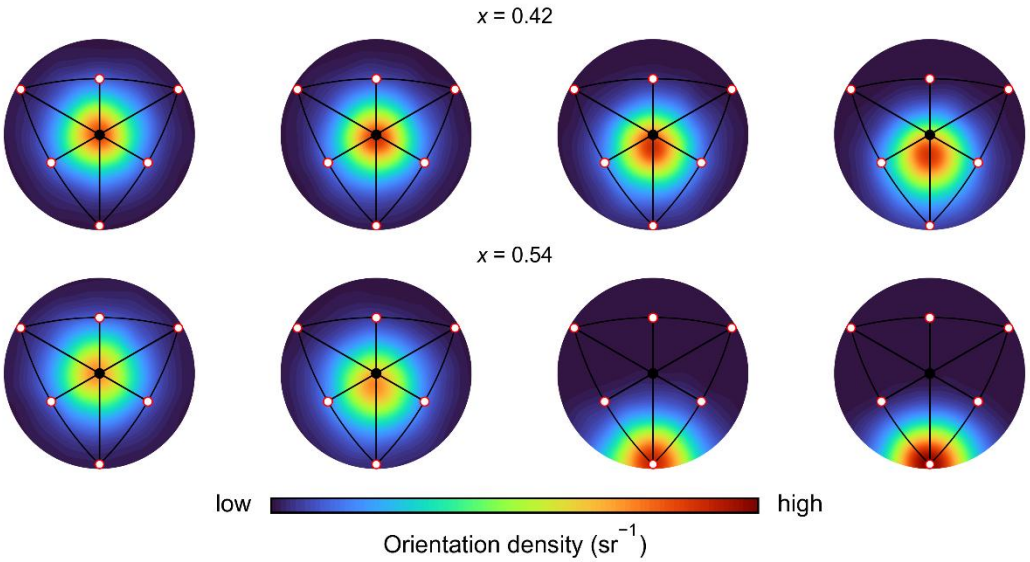
Supplementary Figure 5. Angular classification of local rotational hopping events in PZT. (A-F) Numbers of detected hopping events as a function of temperature for x = 0.12, 0.20, 0.30, 0.40, 0.50 and 0.56, respectively. Events are classified by the angular separation between consecutive valid assigned $\langle 111 \rangle_p$ states: approximately 71°, 109° or 180°. Counts are accumulated over all octahedra within the 25-ps observation window using the smoothing and filtering criteria described in Methods; invalid frames are skipped when comparing successive valid states.



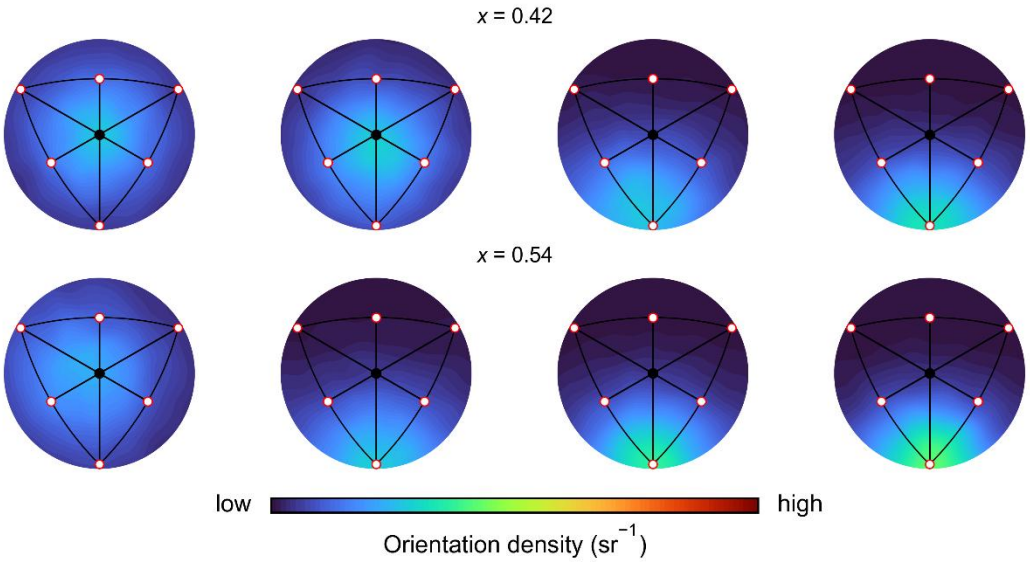
Supplementary Figure 6. Sensitivity of the characteristic temperatures to the hopping-fraction thresholds. (A) Composition dependence of T_{R1} determined using upper thresholds of f_{hop} = 0.85, 0.90 and 0.95. (B) Composition dependence of T_{R2} determined using lower thresholds of f_{hop} = 0.05, 0.10 and 0.15. Each characteristic temperature is identified as the first sampled temperature at which the hopping fraction falls below the corresponding threshold upon cooling. Black curves indicate the thresholds adopted in the main text; shaded regions span the results obtained with the alternative thresholds.



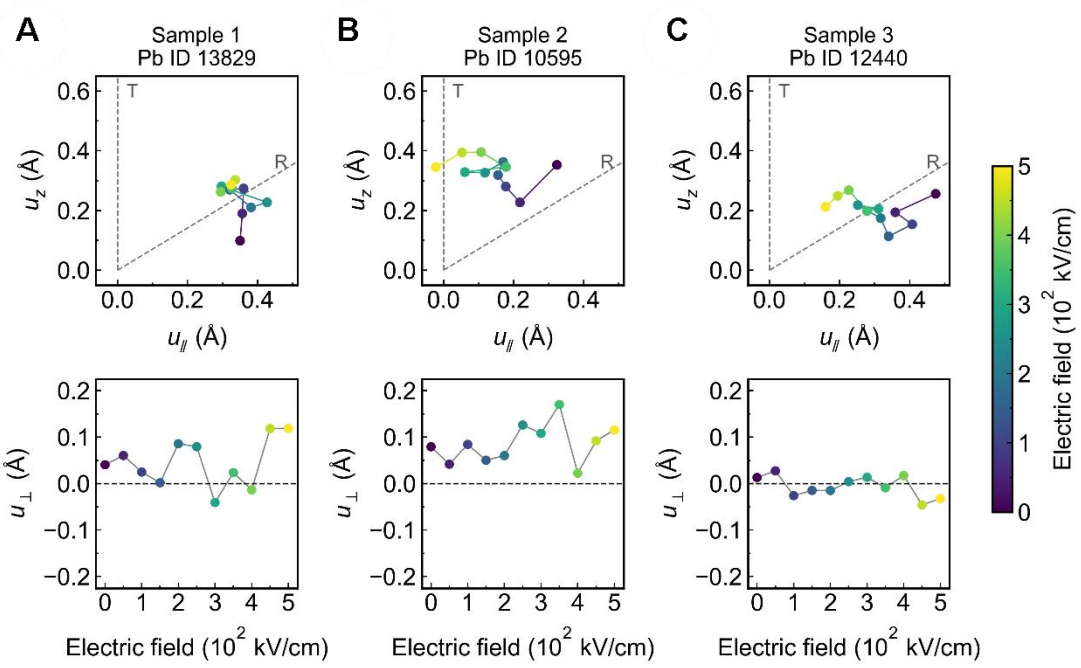
Supplementary Figure 7. Composition dependence of rotational hopping and sensitivity to heating/cooling conditions. (A) Comparison of hopping-fraction curves obtained during heating and cooling at 1 K/ps and cooling at 0.5 and 0.2 K/ps for x = 0.4. (B) Temperature dependence of the hopping fraction f_{hop} for x = 0.12, 0.30 and 0.56. All hopping fractions are evaluated using the same 25-ps observation window and state-assignment criteria. Horizontal dashed lines indicate f_{hop} = 0.9 and 0.1.



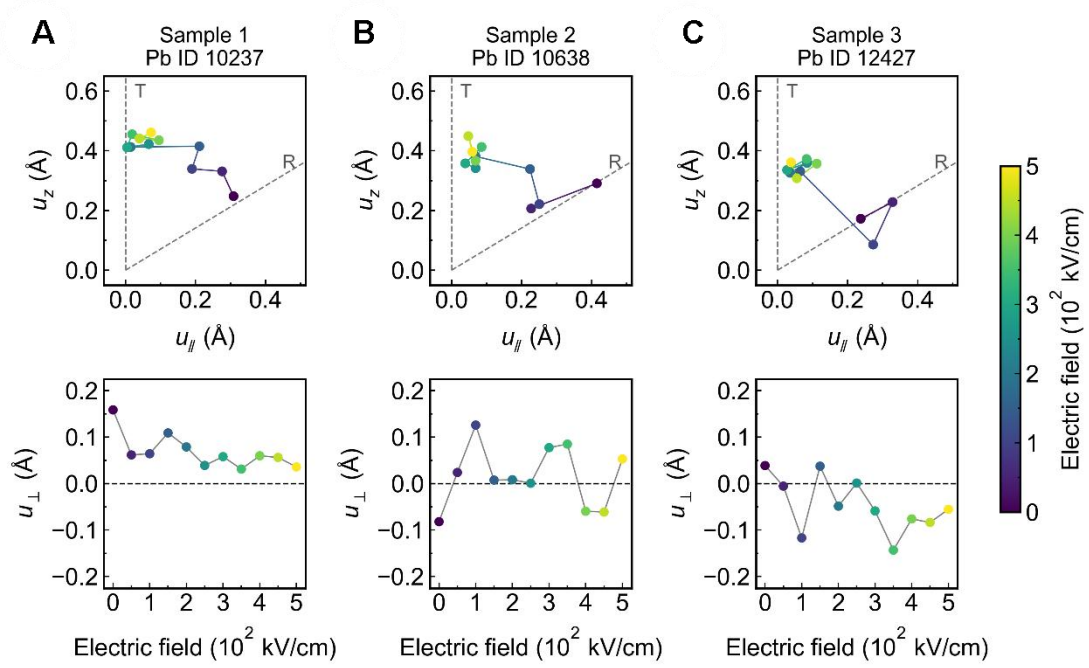
Supplementary Figure 8. Field-dependent Pb displacement orientations at 200 K. Orientational probability density maps of instantaneous Pb off-centre displacement vectors for $x = 0.42$ (top row) and $x = 0.54$ (bottom row). Columns correspond, from left to right, to electric fields of 0, 100, 300 and 500 kV/cm applied along $[001]_p$. Each distribution includes all Pb sites in the final equilibrated frame at the corresponding field strength, without temporal averaging. Probability densities are estimated on the unit sphere using spherical kernel density estimation and displayed by stereographic projection. Colours represent probability density per unit solid angle (sr^{-1}). Reference directions follow Figure 8A.



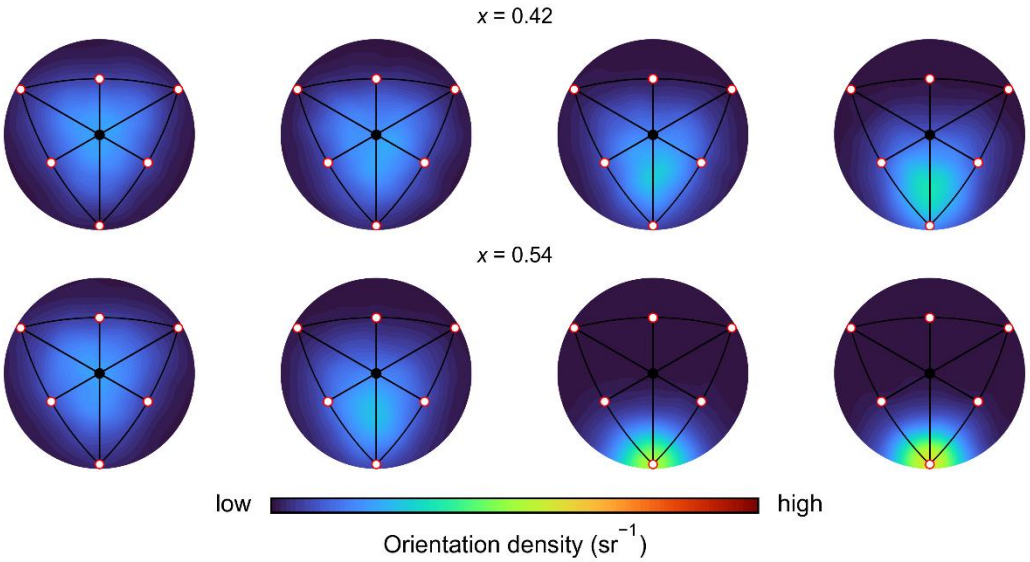
Supplementary Figure 9. Field-dependent Pb displacement orientations at 400 K. Orientational probability density maps of instantaneous Pb off-centre displacement vectors for $x = 0.42$ (top row) and $x = 0.54$ (bottom row), under electric fields of 0, 100, 300 and 500 kV/cm from left to right. The field is applied along $[001]_p$. Distributions are calculated from all Pb sites in the final equilibrated frame at each field strength, without temporal averaging. Spherical kernel density estimates are displayed by stereographic projection, with colours representing probability density per unit solid angle (sr^{-1}). Reference directions follow Figure 8A.



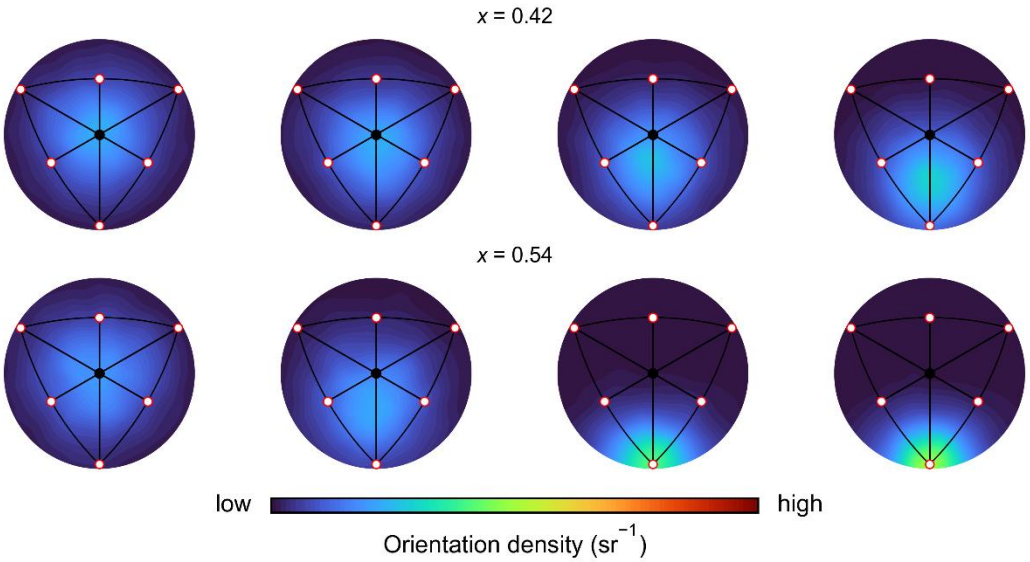
Supplementary Figure 10. Field-dependent displacements of selected Pb sites in PZT with $x = 0.42$. (A-C) One Pb site selected from each of three independent simulation replicas at 300 K, with site identifiers indicated above the panels. The same site is tracked across successive electric-field increments along $[001]_p$. At each field strength, the instantaneous displacement vectors are first transformed by taking the absolute values of their x and y components while retaining the signed z component. The transformed vectors are then averaged over 10 saved frames (10 ps). Top panels show the averaged vectors projected onto the $(1\bar{1}0)_p$ plane, which contains the ideal R-like $[111]_p$ and T-like $[001]_p$ directions. The horizontal coordinate $u_{/\!/}$ is the component along $[110]_p$, and the vertical coordinate u_z is the component along the applied field. Bottom panels show the component $u_\perp$ normal to this plane, along $[\bar{1}10]_p$, as a function of electric-field strength. Dashed lines in the top panels indicate the ideal R- and T-like directions. Colours denote electric-field strength. Connecting lines are guides to the eye between successive field strengths and do not represent time-resolved atomic trajectories.



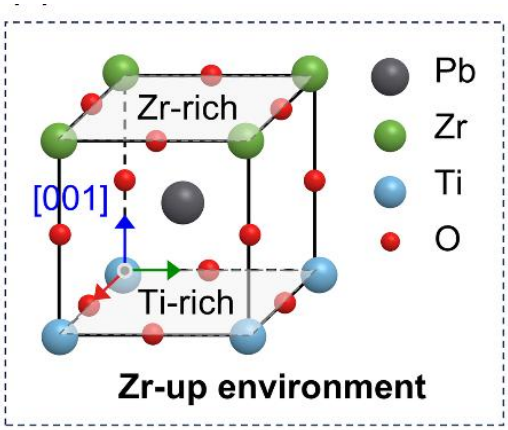
Supplementary Figure 11. Field-dependent displacements of selected Pb sites in PZT with $x = 0.54$. (A-C) One Pb site selected from each of three independent simulation replicas at 300 K, with site identifiers indicated above the panels. The same site is tracked across successive electric-field increments along $[001]_p$. At each field strength, the instantaneous displacement vectors are first transformed by taking the absolute values of their x and y components while retaining the signed z component. The transformed vectors are then averaged over 10 saved frames (10 ps). Top panels show the averaged vectors projected onto the $(1\bar{1}0)_p$ plane, which contains the ideal R-like $[111]_p$ and T-like $[001]_p$ directions. The horizontal coordinate $u_{/\!/}$ is the component along $[110]_p$, and the vertical coordinate u_z is the component along the applied field. Bottom panels show the component $u_\perp$ normal to this plane, along $[\bar{1}10]_p$, as a function of electric-field strength. Dashed lines in the top panels indicate the ideal R- and T-like directions. Colours denote electric-field strength. Connecting lines are guides to the eye between successive field strengths and do not represent time-resolved atomic trajectories.



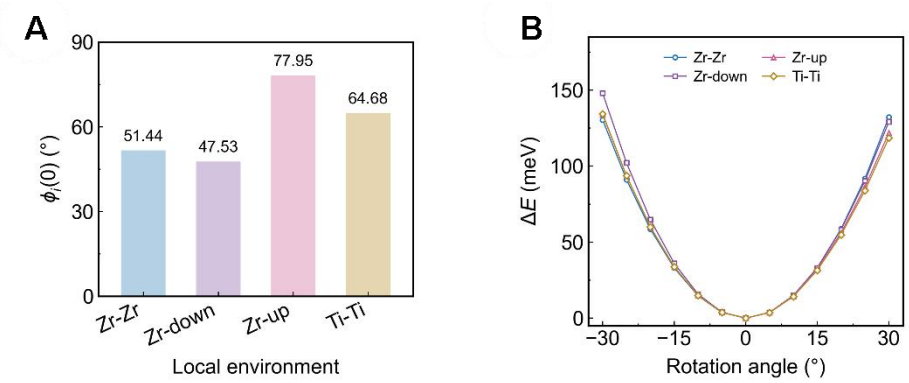
Supplementary Figure 12. Field-dependent Ti displacement orientations at 300 K. Orientational probability density maps of instantaneous Ti off-centre displacement vectors for $x = 0.42$ (top row) and $x = 0.54$ (bottom row). Columns correspond, from left to right, to electric fields of 0, 100, 300 and 500 kV/cm applied along $[001]_p$. Each distribution includes all Ti sites in the final equilibrated frame at the corresponding field strength, without temporal averaging. Probability densities are estimated on the unit sphere using spherical kernel density estimation and displayed by stereographic projection. Colours represent probability density per unit solid angle (sr^{-1}). Reference directions follow Figure 8A.



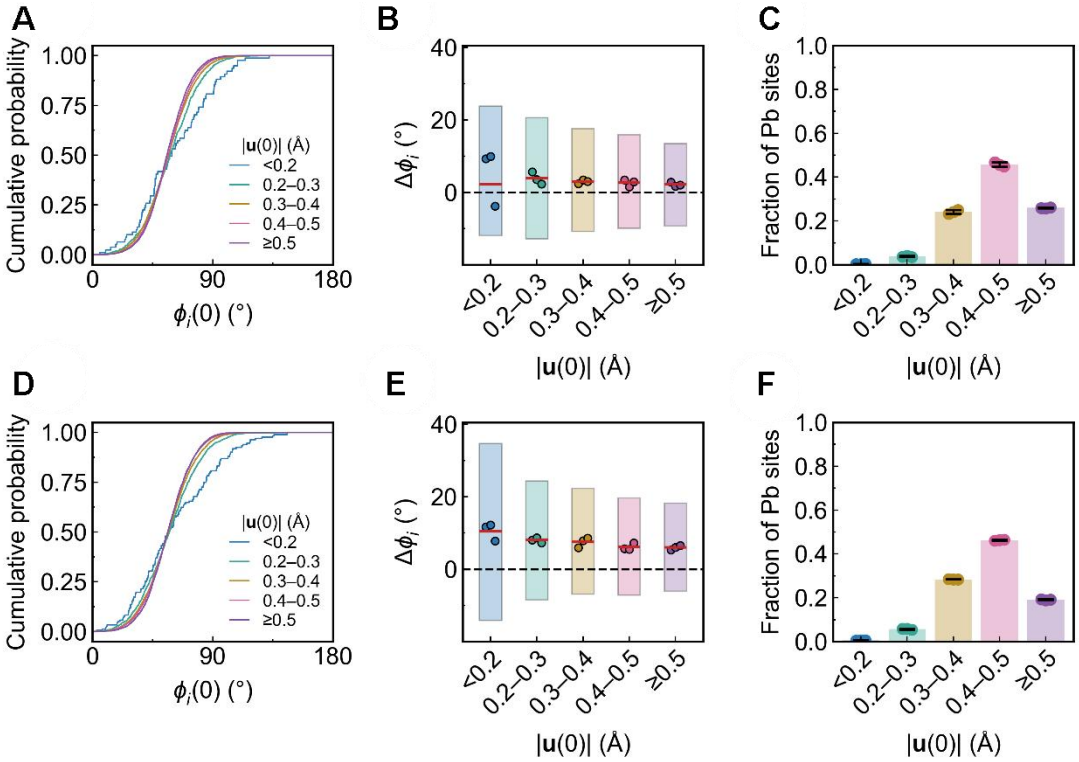
Supplementary Figure 13. Field-dependent Zr displacement orientations at 300 K. Orientational probability density maps of instantaneous Zr off-centre displacement vectors for $x = 0.42$ (top row) and $x = 0.54$ (bottom row). Columns correspond, from left to right, to electric fields of 0, 100, 300 and 500 kV/cm applied along $[001]_p$. Each distribution includes all Zr sites in the final equilibrated frame at the corresponding field strength, without temporal averaging. Probability densities are estimated on the unit sphere using spherical kernel density estimation and displayed by stereographic projection. Colours represent probability density per unit solid angle (sr^{-1}). Reference directions follow Figure 8A.



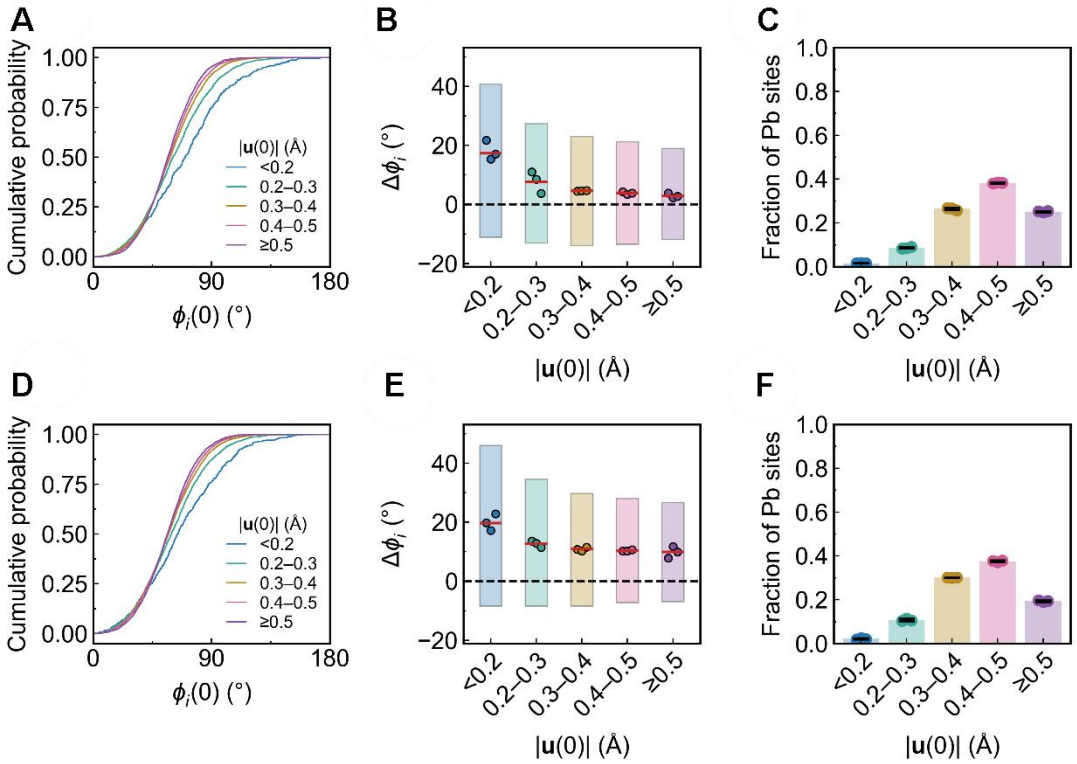
Supplementary Figure 14. Definition of the local chemical environment around a Pb site. Representative Zr-up configuration illustrating the two pseudo-cubic $(001)_p$ planes formed by the eight nearest Zr/Ti neighbours of Pb. Each plane contains four Zr/Ti sites and is classified as Zr-rich when at least three are occupied by Zr. Zr-up and Zr-down denote environments with a single Zr-rich plane above and below Pb, respectively; Zr-Zr denotes two Zr-rich planes; and other-environments contain no Zr-rich plane under this criterion. Above and below refer to the positive and negative z directions, respectively. The applied-field direction is $[001]_p$.



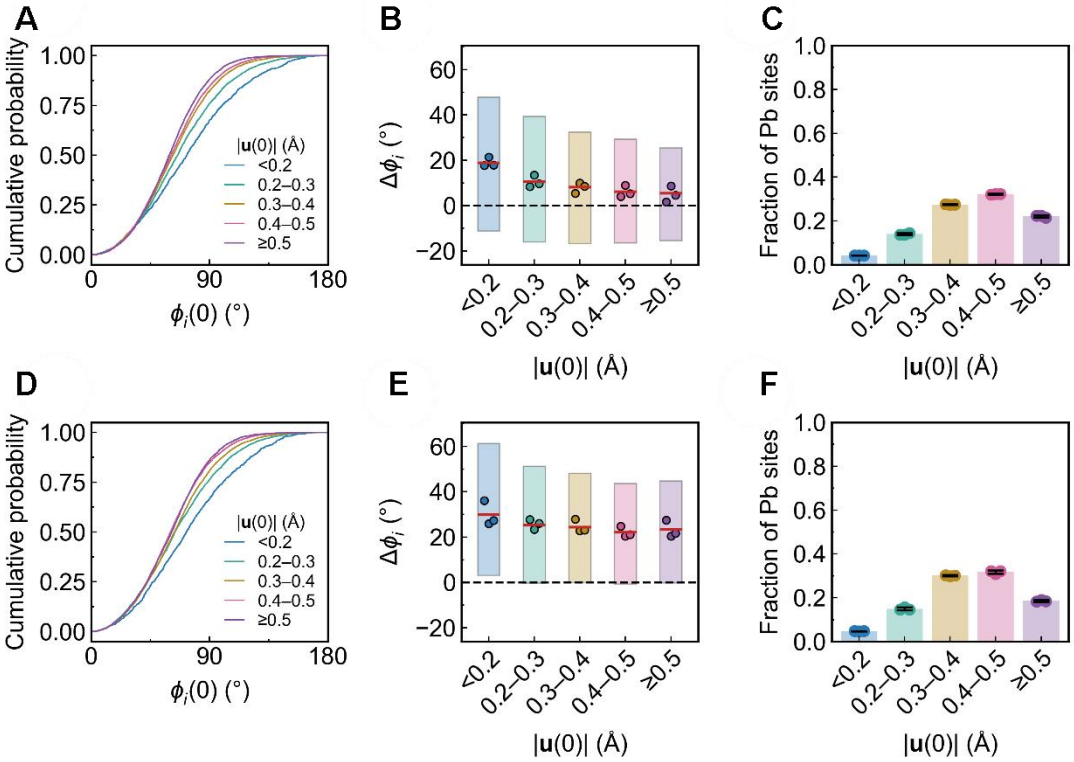
Supplementary Figure 15. Constrained Pb-displacement rotation-energy profiles for selected local chemical environments in PZT with x = 0.40. Representative Pb sites are selected after energy minimization of an equilibrated configuration obtained from a zero-field trajectory at 300 K. Unlike the statistical classification in Figure 10, each neighbouring plane in these examples contains four atoms of the same species. Zr-Zr and Ti-Ti denote two all-Zr and two all-Ti planes, respectively; Zr-up and Zr-down denote an all-Zr plane above or below Pb, with an all-Ti plane on the opposite side. (A) Initial deviation angles between the minimized Pb-displacement vectors and $[001]_p$. (B) NEP single-point energy changes upon rotating each selected Pb-displacement vector within the plane spanned by its initial direction and $[001]_p$. The displacement magnitude, approximately 0.4 Å, is held fixed for each site, together with all other atomic positions and the simulation cell. Positive and negative rotation angles correspond to rotation towards and away from $[001]_p$, respectively. Energy changes are referenced to the corresponding unrotated configuration. No structural relaxation is performed during the rotation scans.



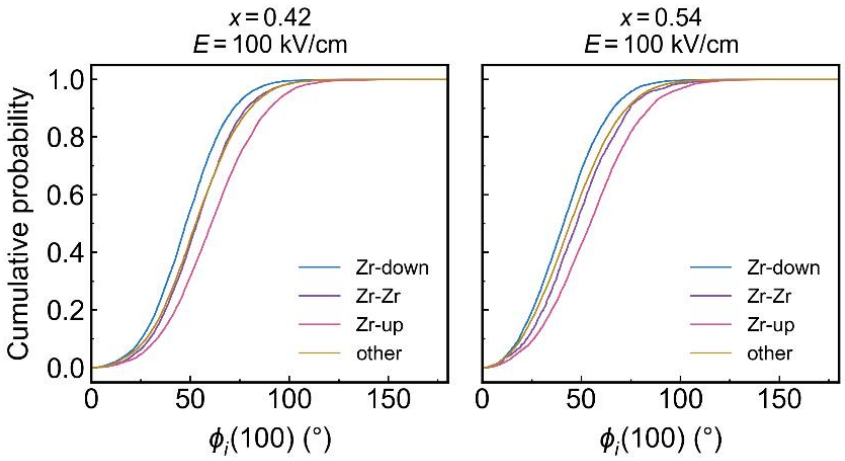
Supplementary Figure 16. Dependence of Pb angular responses on the initial displacement magnitude at 200 K. (A-C) x = 0.42, (D-F) x = 0.54. Pb sites are grouped according to their zero-field displacement magnitude $|\mathbf{u}(0)|$ into five intervals: < 0.2, 0.2-0.3, 0.3-0.4, 0.4-0.5, and ≥ 0.5 Å. Intermediate intervals include their lower bounds and exclude their upper bounds. (A and D) Cumulative distributions of the zero-field deviation angle $\phi(0)$ relative to $[001]_p$. (B and E) Site-resolved angular changes, $\Delta\phi=\phi(0)-\phi(100)$, upon increasing the field from 0 to 100 kV/cm along $[001]_p$. Positive values indicate rotation towards the field. Shaded boxes span the 25th–75th percentiles, red horizontal lines indicate medians, and circles show the median values from three independent simulation replicas. Dashed horizontal lines mark $\Delta\phi$ = 0. (C and F) Fractions of Pb sites in each displacement-magnitude interval. Bars show the mean fractions across three independent simulation replicas, circles indicate the values for individual replicas, and black error bars represent the standard deviation. Displacements are calculated from the final equilibrated frame at each field strength. All displacement-magnitude groups are included in this analysis.



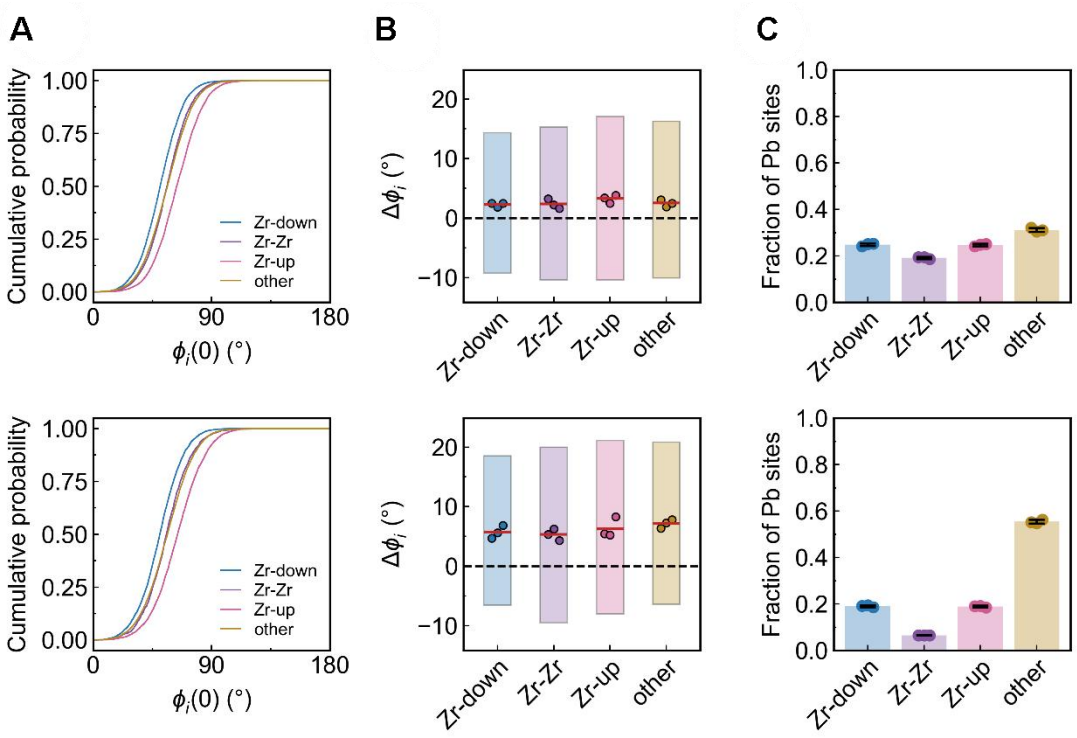
Supplementary Figure 17. Dependence of Pb angular responses on the initial displacement magnitude at 300 K. (A-C) x = 0.42, (D-F) x = 0.54. Pb sites are grouped according to their zero-field displacement magnitude $|\mathbf{u}(0)|$ into five intervals: < 0.2, 0.2-0.3, 0.3-0.4, 0.4-0.5, and ≥ 0.5 Å. Intermediate intervals include their lower bounds and exclude their upper bounds. (A and D) Cumulative distributions of the zero-field deviation angle $\phi(0)$ relative to $[001]_p$. (B and E)Site-resolved angular changes, $\Delta\phi=\phi(0)-\phi(100)$, upon increasing the field from 0 to 100 kV/cm along $[001]_p$. Positive values indicate rotation towards the field. Shaded boxes span the 25th–75th percentiles, red horizontal lines indicate medians, and circles show the median values from three independent simulation replicas. Dashed horizontal lines mark $\Delta\phi$ = 0. (C and F) Fractions of Pb sites in each displacement-magnitude interval. Bars show the mean fractions across three independent simulation replicas, circles indicate the values for individual replicas, and black error bars represent the standard deviation. Displacements are calculated from the final equilibrated frame at each field strength. All displacement-magnitude groups are included in this analysis.



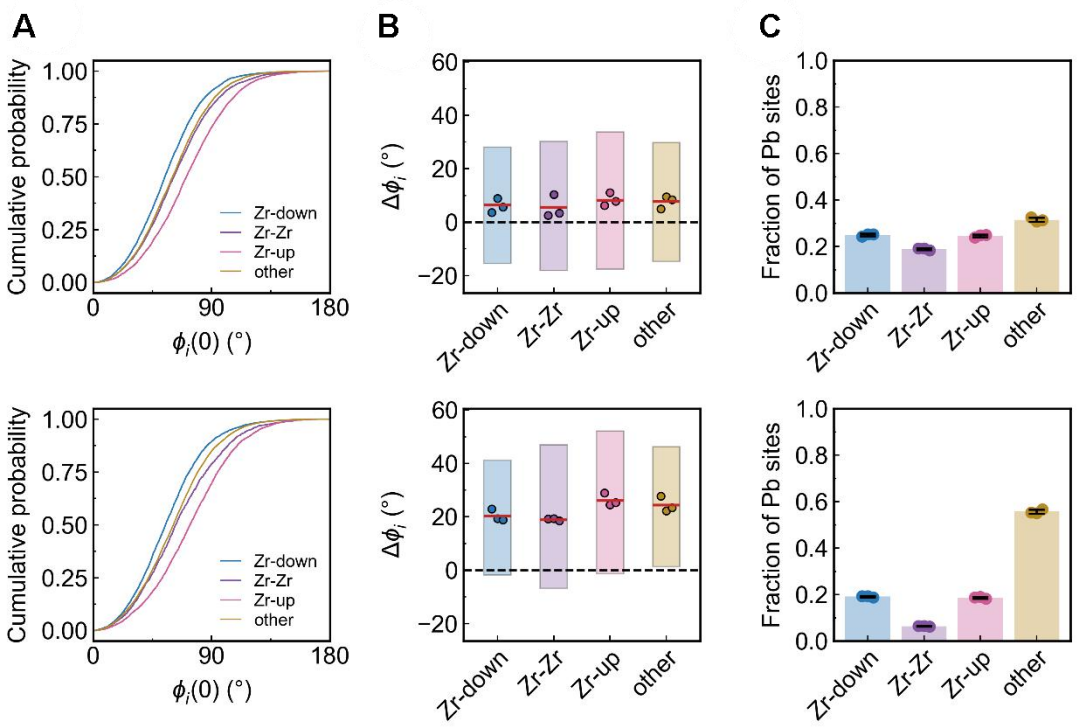
Supplementary Figure 18. Dependence of Pb angular responses on the initial displacement magnitude at 400 K. (A-C) x = 0.42, (D-F) x = 0.54. Pb sites are grouped according to their zero-field displacement magnitude $|\mathbf{u}(0)|$ into five intervals: < 0.2, 0.2-0.3, 0.3-0.4, 0.4-0.5, and ≥ 0.5 Å. Intermediate intervals include their lower bounds and exclude their upper bounds. (A and E) Cumulative distributions of the zero-field deviation angle $\phi(0)$ relative to $[001]_p$. (B and E) Site-resolved angular changes, $\Delta\phi=\phi(0)-\phi(100)$, upon increasing the field from 0 to 100 kV/cm along $[001]_p$. Positive values indicate rotation towards the field. Shaded boxes span the 25th–75th percentiles, red horizontal lines indicate medians, and circles show the median values from three independent simulation replicas. Dashed horizontal lines mark $\Delta\phi$ = 0. (C and F) Fractions of Pb sites in each displacement-magnitude interval. Bars show the mean fractions across three independent simulation replicas, circles indicate the values for individual replicas, and black error bars represent the standard deviation. Displacements are calculated from the final equilibrated frame at each field strength. All displacement-magnitude groups are included in this analysis.



Supplementary Figure 19. Local-environment-resolved Pb-displacement orientations at 100 kV/cm and 300 K. Cumulative distributions of the deviation angle $\phi(100)$ between the local Pb off-centre displacement and an electric field applied along $[001]_p$, for x = 0.42 (left) and x = 0.54 (right). Colours distinguish Zr-down, Zr–Zr, Zr-up and other environments, as defined in Figure 10. Distributions are calculated from the final equilibrated frame at 100 kV/cm for sites selected by the zero-field criterion ($|\mathbf{u}(0)| \geq 0.2$ Å). A shift towards smaller angles indicates closer alignment with the field.



Supplementary Figure 20. Local chemical dependence of Pb-displacement orientations and field-induced reorientation at 200 K. The upper and lower rows show results for $x = 0.42$ and $x = 0.54$, respectively. (A) Cumulative distributions of the zero-field deviation angle $\phi(0)$ between the local Pb off-centre displacement and $[001]_p$, resolved into Zr-down, Zr-Zr, Zr-up and other-environments as defined in the text. (B) Site-resolved angular changes, $\Delta\phi=\phi(0)-\phi(100)$, upon increasing the electric field from 0 to 100 kV/cm along $[001]_p$. Positive values indicate rotation towards the field direction. Shaded boxes span the 25th–75th percentiles, red horizontal lines indicate medians, and circles show the median values from three independent simulation replicas. Dashed horizontal lines mark $\Delta\phi = 0$. (C) Fractions of Pb sites belonging to each local-environment category. Angular quantities are calculated from the final equilibrated frame at each field strength, retaining the same Pb sites selected by the zero-field criterion ($|\mathbf{u}(0)| \geq 0.2$ Å). Bars show the mean fractions across three independent simulation replicas, circles indicate the values for individual replicas, and black error bars represent the standard deviation.



Supplementary Figure 21. Local chemical dependence of Pb-displacement orientations and field-induced reorientation at 400 K. The upper and lower rows show results for $x = 0.42$ and $x = 0.54$, respectively. (A) Cumulative distributions of the zero-field deviation angle $\phi(0)$ between the local Pb off-centre displacement and $[001]_p$, resolved into Zr-down, Zr-Zr, Zr-up and other-environments as defined in the text. (B) Site-resolved angular changes, $\Delta\phi=\phi(0)-\phi(100)$, upon increasing the electric field from 0 to 100 kV/cm along $[001]_p$. Positive values indicate rotation towards the field direction. Shaded boxes span the 25th–75th percentiles, red horizontal lines indicate medians, and circles show the median values from three independent simulation replicas. Dashed horizontal lines mark $\Delta\phi = 0$. (C) Fractions of Pb sites belonging to each local-environment category. Angular quantities are calculated from the final equilibrated frame at each field strength, retaining the same Pb sites selected by the zero-field criterion ($|\mathbf{u}(0)| \geq 0.2$ Å). Bars show the mean fractions across three independent simulation replicas, circles indicate the values for individual replicas, and black error bars represent the standard deviation.

Supplementary Table

Supplementary Table 1. Comparison of the accuracy of NEP models with different radial and angular cutoff combinations, evaluated using the root-mean-square errors (RMSE) of energies, atomic forces, and virials

Cutoff (Å) (radial, angular)	**Energy RMSE (eV/atom)**	**Force RMSE (eV/Å)**	**Virial RMSE (eV/atom)**
(6, 4)	0.00086	0.07940	0.02108
(8, 4)	0.00093	0.08010	0.02227
(10, 4)	0.00096	0.08172	0.02169
(8, 6)	0.00080	0.06353	0.02053
(10, 6)	0.00085	0.06494	0.02289
(10, 8)	0.00086	0.06710	0.02107

All models were trained using the initial dataset of $x = 0.5$.